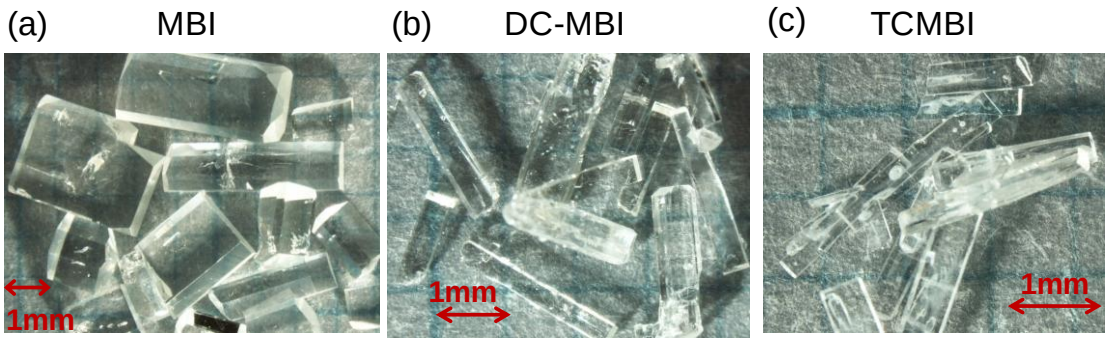

Supplementary Figure S1: Photographs of single crystals. (a) MBI, (b) DC-MBI, and (c) TCMBI.

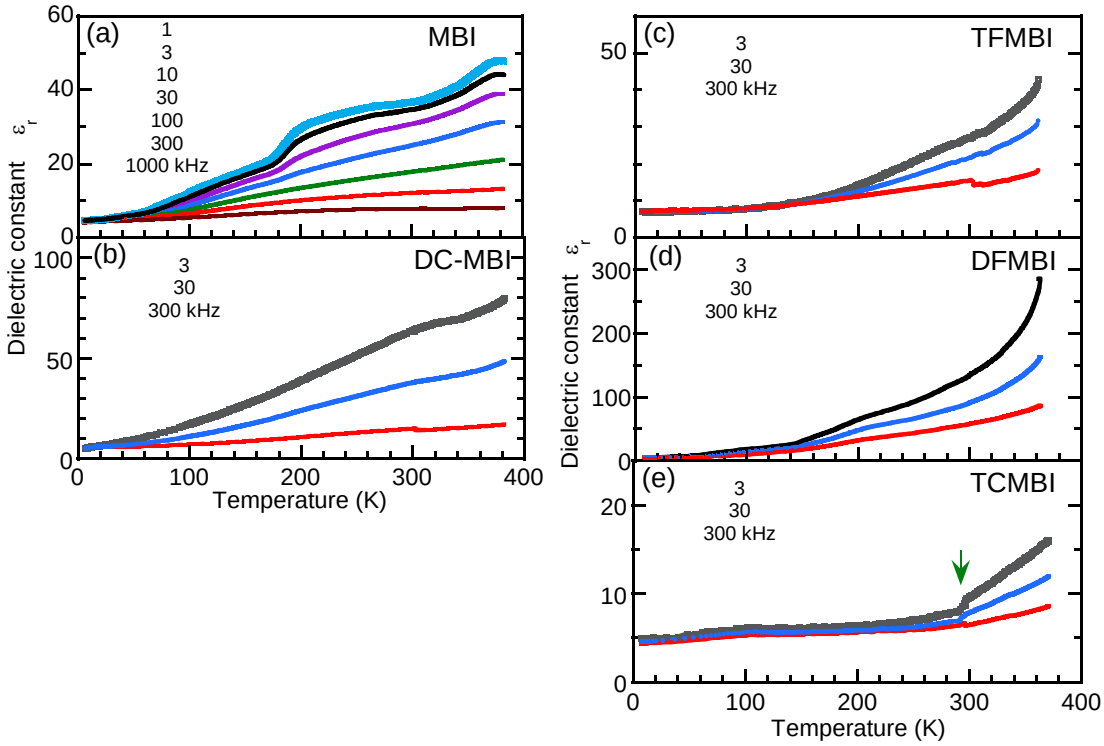

Supplementary Figure S2: Temperature dependence of relative permittivity ε_r. (a) MBI, (b) DC-MBI, (c) TFMBI, (d) DFMBI, and (e) TCMBI crystals in the cooling cycle. The electric field was applied parallel to the directions of hydrogen-bonded molecular sequence.

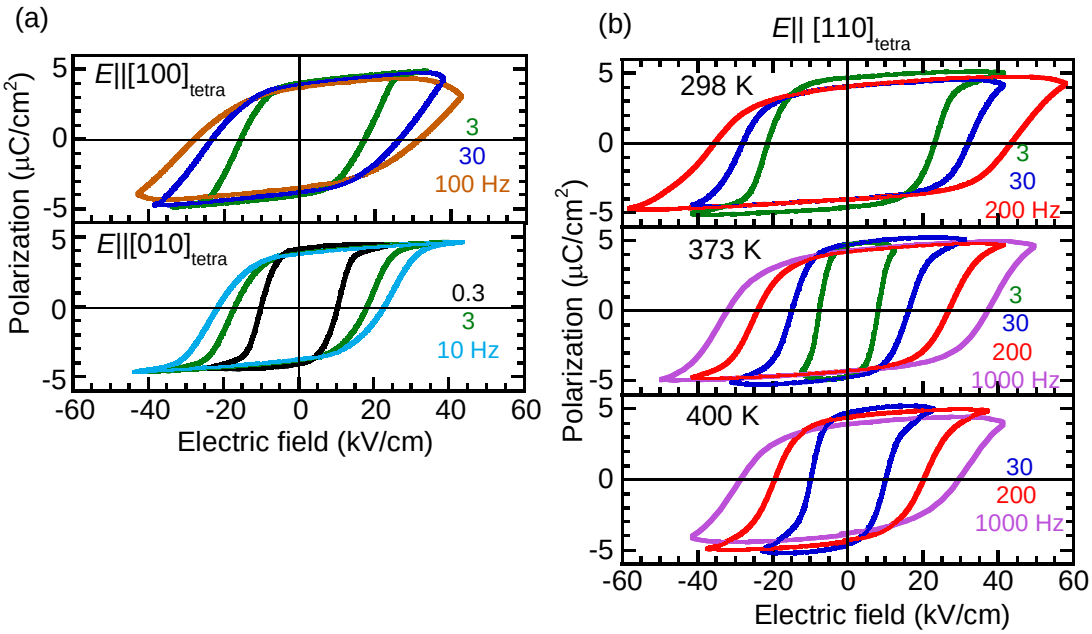

Supplementary Figure S3: Ferroelectric properties of MBI. (a) The $[100]_{tetra}$ and $[010]_{tetra}$ -direction polarization (*P*) vs. electric field (*E*) hysteresis loops at room temperature. (c) The $[110]_{tetra}$ -direction polarization (*P*) vs. electric field (*E*) hysteresis loops at various temperatures (298 K, 373 K, and 400 K) measured with triangular ac electric field of various frequencies.

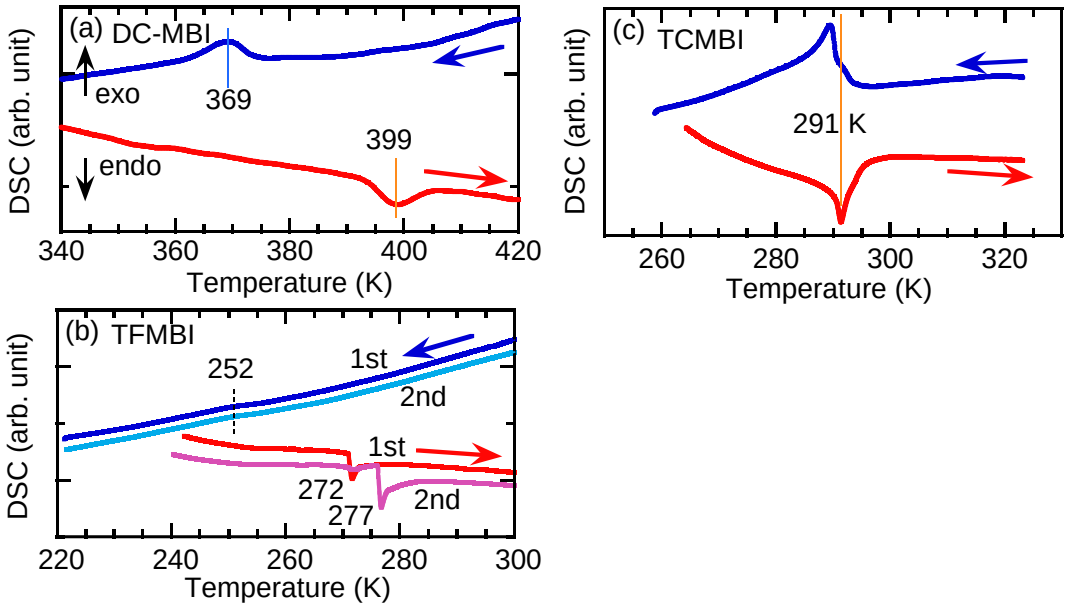

Supplementary Figure S4: Differential scanning calorimetry (DSC). (a) DC-MBI, (b) TFMBI, and (c) TCMBI powder. The DSC of TFMBI depends on the thermal history, as shown by the data of the first and second cooling/heating cycles.

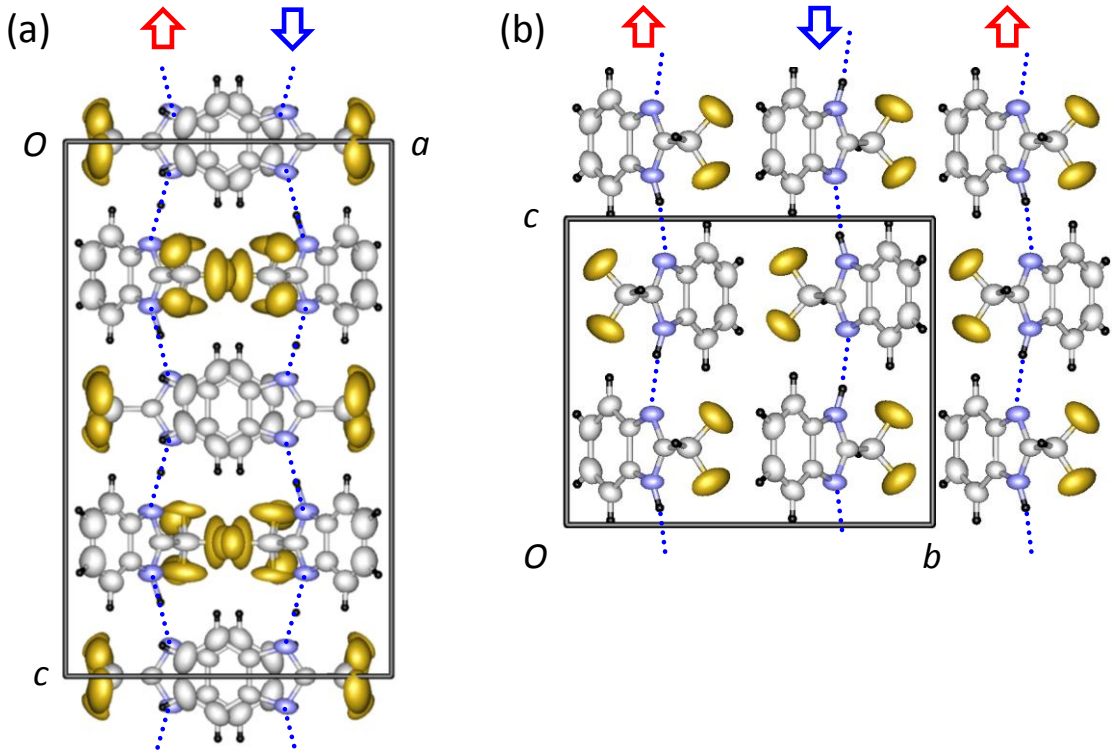

Supplementary Figure S5: Crystal structures. (a) TFMBI, (b) DFMBI.

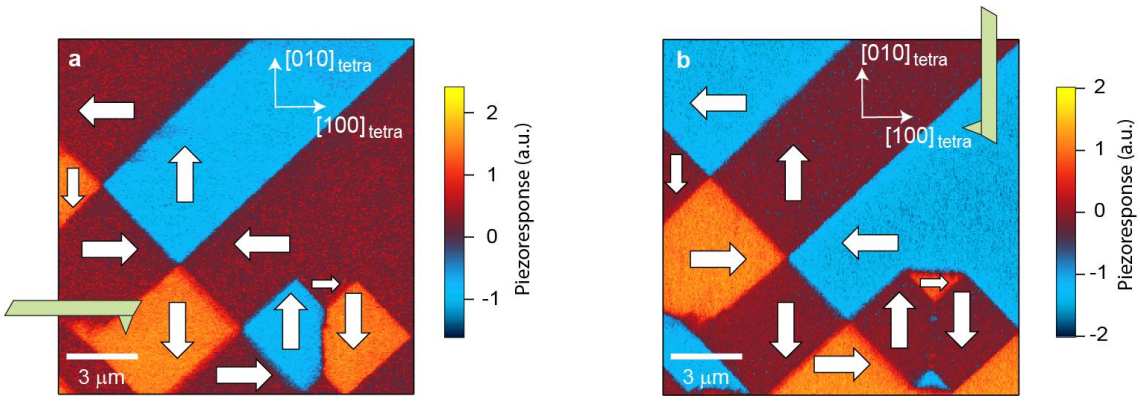

Supplementary Figure S6: In-plane PFM images of MBI $[001]_{tetra}$ surface measured under distinct geometry of cantilever. Local polarization directions (white arrows) and cantilever geometry are indicated schematically.

	MBI	TCMBI	TFMBI	DFMBI	DC-MBI
chemical formula	$C_9H_8N_2$	$C_8H_5Cl_3N_2$	$C_8H_8F_3N_2$	$C_8H_6F_2N_2$	$C_8H_6Cl_2N_2$
formula wt	144.18	235.50	186.14	168.15	201.07
Temperature /K	300	300	300	295	295
a/ Å	13.9639(3)	10.038(4)	11.856(4)	6.2322(12)	14.238(3)
b/ Å	7.2107(2)	7.059(3)	7.243(2)	12.072(2)	5.6866(12)
c/ Å	13.9639(3)	14.259(7)	19.547(5)	10.1114(19)	10.398(2)
β/deg	90.0	90.0	90.0	90.310(5)	90.0
V/ Å^3	1406.02(6)	1010.4(8)	1678.6(9)	760.7(3)	841.9(3)
Crystal system	monoclinic	monoclinic	monoclinic	monoclinic	orthorhombic
space group	*Pn* (#7)	$P2_1$ (#4)	$P2_1$/c (#14)	$P2_1$/c (#14)	$Pca2_1$ (#29)
ρ_{calc}/ g cm^{-3}	1.249	1.548	1.473	1.468	1.586
Z	8	4	8	4	4
dimensions / mm	0.25×0.15×0.02	0.90×0.25×0.05	0.25×0.05×0.02	0.25×0.20×0.09	0.33×0.32×0.16
radiation	Synchrotron radiated x-ray (λ = 0.9995 Å)	Synchrotron radiated x-ray (λ = 0.6878 Å)	Synchrotron radiated x-ray (λ = 0.9995 Å)	MoKα	MoKα
$2\theta_{max}$/deg	141.1	82.8	135.3	55	55
R_{int}	0.024	0.021	0.058	0.0236	0.0507
reflcn used ($2\sigma(I)<I$)	12811	4770	5176	1718	1819
no. of variables	491	307	305	117	113
R	0.0459	0.0603	0.0309	0.0638	0.0427
R_w	0.0554	0.0847	0.0372	0.1818	0.1487
GOF	0.970	1.075	1.030	1.044	1.127
d_{NN} (intermolecular) / Å	2.8611(16) 2.9607(17) 2.8570(18) 2.9685(15)	2.802(4) 2.806(4)	2.861(3) 2.874(3)	2.851(3)	2.977(4)
$\angle_{NH\cdot\cdot N}$ (intermolecular) / deg	174.1(7) 174.1(6) 172.6(6) 179.5(7)	143.9(8) 157.5(7)	172.9(9) 177.0(6)	161(3)	145(3)

Supplementary Table S1: Crystal data, experimental details, and hydrogen-bonding geometry for the single crystals of ferroelectric and antiferroelectric imidazoles at room temperature.

Supplementary Discussion

Electric properties

All the benzimidazoles used for experiments are purified into colorless crystals, as demonstrated by Supplementary Figure S1. The temperature dependent permittivity is plotted in Supplementary Figure S2. The ac electric field was applied parallel to the dipolar chains. For all the benzimidazoles, the permittivity simply increases with temperature at least up to 360-380 K without a peak anomaly indicative of the Curie point. Thereby, the ferro- or antiferroelectric phase appeared to persist up to far above room temperature. For the TCMBI crystal (Supplementary Figure S2e), a kink-like anomaly is noticed just below room temperature (~ 290 K), and can be related to the phase transition detected also in the calorimetric measurements below.

Considering the crystal symmetry, the perfectly oriented (single-domain) state of MBI generates a spontaneous polarization parallel to either the $[100]_{tetra}$ or $[100]_{tetra}$ axis. Therefore, we examined the dielectric hysteresis at room temperature with configurations of both $E||[100]_{tetra}$ and $E||[010]_{tetra}$ on the same single crystal by cutting it off into two pieces. As shown by Supplementary Figure S3a, very similar remanent polarizations and coercive fields manifest themselves the isotropic nature of ferroelectricity in two dimensions. The coercive field should be minimized for the measurements along the principal polarization vector. Actually, the coercive fields of $E_{c[100]}$ = 16.4 kV/cm and $E_{c[010]}$ = 17.6 kV/cm at f = 3 Hz (Supplementary Figure S3a) are much lower than that (Supplementary Figure S3b) of $E_{c[110]}$ = 22.2 kV/cm, which is consistent with the expected relation, $E_{c[110]} = \sqrt{2}E_{c[100]}$ (~ 23.2 kV/cm). On the other hand, remanent polarizations measured along the principal polarization axes ($P_{r[100]}$ and $P_{r[010]}$ of 3.9-4.0 μC/cm^2) are lower than $P_{r[110]}$ of 5.2 μC/cm^2. The most plausible reason is that the actual crystal is a multi-domains state, and for instance, the $E||[100]_{tetra}$ configuration cannot switch the domains having its normal polarities {i.e. $P||[010]_{tetra}$}, whereas the oblique (45°) configuration of $E||[110]_{tetra}$ can switch all the polar domains. From the latter experiments, the magnitude of full polarization along the principal axis can be evaluated as $\sqrt{2}P_{r[110]}$ = 7.4 μC/cm^2, which is almost twice the observed $P_{r[100]}$. This observation indicates that perpendicular domains have almost the same volume fractions in the crystal used.

The *P*-*E* hysteresis experiments confirmed the ferroelectricity of MBI even at higher temperatures up to 400 K (Supplementary Figure S3b). Although the crystal specimen used for high-temperature experiments is different from that for Fig. 2a, the remanent polarization of 5.0 μC/cm^2 almost coincides that optimized one (5.2 μC/cm^2). We found little temperature changes of remanent polarization, whereas the linear decrease of coercive field with temperature suggests the possible disappearance of ferroelectricity at higher temperature beyond 400 K.

Thermal properties

The differential scanning calorimetry confirmed the absence of anomalies indicative of the Curie point T_c above room temperature until the solids gradually start to sublime; the ferroelectric MBI (T_c > 430 K, sample weight of 15.74 mg), antiferroelectric DFMBI (> 413 K, 11.24 mg), TFMBI (> 393 K, 17.46 mg), and TCMBI (> 413 K, 4.31 mg). On the other hand, the ferroelectric DC-MBI (23.31 mg) exhibited an exothermic peak on cooling and an endothermic peak on heating at 369 and 399 K, respectively (Supplementary Figure S4a). The large thermal hysteresis indicates a strong first order nature of the phase transition. We also noticed that some structural changes other than Curie temperature for TFMBI (Supplementary Figure S4b) and TCMBI (Supplementary Figure S4c), as revealed by the endothermic peak lying just below room temperature. The TFMBI crystal exhibited a broad exothermic anomaly around 252 K and sharp endothermic peaks, which appear to depend on thermal history. The TCMBI crystal exhibited a couple of exothermic and endothermic peaks at 291 K, in agreement with the kink-like anomaly of permittivity. These anomalies indicate some structural changes, which might involve the CCl_3 and CF_3 groups in rotational disorder, respectively. Their detailed nature is beyond the scope of this paper and then remains for future work along with the other experimental characterizations.

X-ray crystallographic data

Supplementary Table S1 summarizes the crystal data, experimental details, and hydrogen-bonding geometry for five benzimidazoles according to the x-ray diffraction experiments performed at room temperature. Supplementary Figure S5 depicts the antipolar arrangements of hydrogen-bonded chains in the antiferroelectric TFMBI and DFMBI crystals.

PFM measurements

To identify the direction of local polarization $\boldsymbol{P}_{\mathrm{local}}$ in MBI, the in-plane PFM images were collected under different cantilever geometries, as shown in Supplementary Figures S6a and S6b. Generally, domains hosting $\boldsymbol{P}_{\mathrm{local}}$ parallel to cantilever exhibit vanishingly small in-plane piezoresponse, so directions of $\boldsymbol{P}_{\mathrm{local}}$ can be determined by checking this "extinction rule". From the considerations of crystal structure of MBI, it is reasonable to postulate that $\boldsymbol{P}_{\mathrm{local}}$ is parallel to any of [100], [-110], [010], or [0-10] in the pseudo-tetragonal setting. In Supplementary Figure S6, the dark red area, which exhibits small piezoresponse, can be attributed to domains hosting $\boldsymbol{P}_{\mathrm{local}}$ parallel to the cantilever. On the other hand, orange and light blue areas have relatively large piezoresponse, indicating that $\boldsymbol{P}_{\mathrm{local}}$ are perpendicular to the cantilever. In this way, $\boldsymbol{P}_{\mathrm{local}}$ configurations are determined as shown in Supplementary Figure S6. Note that changing the cantilever geometry by 90 degree converts "dark red" to "orange" (or "light blue") and vice versa between Supplementary Figures S6a and S6b, corroborating our assignment of $\boldsymbol{P}_{\mathrm{local}}$.